Synthesis of Reactively Loaded Sparse Antenna Arrays Using Optimization on Riemannian Manifold

ALBERT SALMI[ID], ANU LEHTOVUORI[ID], AND VILLE VIIKARI[ID] (Senior Member, IEEE)

Department of Electronics and Nanoengineering, Aalto University, 00076 Aalto, Finland

CORRESPONDING AUTHOR: A. SALMI (e-mail: albert.salmi@aalto.fi)

ABSTRACT This paper introduces a method for computing reactive terminations for scatterer elements in antenna arrays. With the fixed scatterer elements, we shape embedded element patterns of sparse arrays to focus the radiation into a grating-lobe-free limited field of view. The reactive terminations of the scatterer elements are determined by optimizing reflection coefficients on a Riemannian manifold. In addition, we show that widening the grating-lobe-free field of view is possible by tilting the field of view. We design both 5-element linear and 4-by-4-element planar reactively loaded antenna arrays with 1.4-wavelength inter-element distances. The terminations of the scatterer elements are optimized so that the arrays cover either the broadside-located or the tilted grating-lobe-free field of view. The results obtained from the linear array are validated through measurements of manufactured prototypes.

INDEX TERMS Antenna arrays, field of view, grating lobes, manifold optimization, reactive scatterers, sparse antenna arrays.

I. INTRODUCTION

AT MILLIMETER-WAVE frequencies and above, radio-frequency integrated circuits (RFICs), which control and feed antenna arrays, become large in wavelengths [1]. As the number of array elements scales up in modern wireless communication and sensing systems, the array elements must be tightly integrated with the RFIC to reduce losses and avoid complex signal routing. Consequently, the array becomes sparse as the RFIC's area per antenna element exceeds half-wavelength. In addition to being forced by modern radio technology, the sparse arrays can be intentionally designed due to their capability for higher scan gain and lower mutual coupling.

As the inter-element distances exceed half-wavelength, grating lobes become an issue. They radiate power to undesired directions and decrease the signal-to-noise ratio. To avoid the emergence of the grating lobes, the field of view (FoV) of the antenna array must be limited [2].

Synthesizing antenna arrays with limited FoVs has gained considerable interest in the antenna community. Recent research has shown that the FoV can be successfully limited by constructing the array elements from fixed sub-arrays [3], [4], [5], [6], [7]. The sub-array approach can be further improved by synthesizing matching circuits for the individual sub-array elements [8]. However, the viability of sub-array techniques depends on the availability of sufficient space for sub-array feeding networks.

The need for sub-array feeding networks can be circumvented by adopting aperture-coupled sub-array elements [5], [9], or parasitic scatterers [10], [11], [12]. In a broader context, the radiation properties of the array can be manipulated with arbitrary passive elements that can be terminated to specific loads. These elements couple to the driven elements and scatter the electromagnetic fields. In a recent study [13], the scatterer elements were arranged in a rectangular lattice on a printed circuit board and terminated to either short or open circuits, resulting in a pixel antenna topology.

The scatterer elements should be terminated so that the superposition of the primary and scattered fields forms the desired radiation properties, such as embedded element patterns (EEPs) toward the limited FoV. In most of the cases, the terminations must be reactive to avoid resistive losses.

In [5], the embedded element patterns are shaped using parasitic scatterers that are implemented with waveguides on the antenna aperture. The lengths of the waveguides are optimized using a genetic algorithm. In [14], a driven dipole antenna is surrounded by reactively terminated dipoles whose terminations are optimized using semi-definite relaxation. The method maximizes the realized gain only towards a single direction, requiring tunable terminations for beam steering.

The state-of-the-art methods for designing reactively loaded antenna arrays primarily utilize genetic algorithms and semi-definite relaxation-based techniques [5], [14], [15], [16]. However, a challenge regarding genetic algorithms is their suitability for large-scale, computationally heavy problems, and semi-definite relaxation does not always yield practically realizable results. Moreover, the semi-definite relaxation-based methods have not been applied for beam-steerable antenna arrays with fixed reactively terminated scatterers. Determining the fixed scatterer terminations for beam-steerable antenna arrays is computationally demanding and lacks a universally straightforward approach.

In radio sciences, optimization on a Riemannian manifold has been used successfully for designing radar beampatterns [17], [18], [19]. It has also been used for radio interferometric calibration [20], radio device rotational orientation estimation [21], and configuration of reconfigurable intelligent surfaces [22]. In quantum technologies, the feasibility of manifold optimization has been demonstrated in quantum gate decomposition and quantum tomography [23]. In addition, these methods have been applied widely in data science and machine learning [24], [25], [26].

In this paper, we present an application of manifold optimization to determine the terminations of arbitrarily placed, beam-independent reactive scatterers. The optimization algorithm uses the gradient of the objective function, which significantly improves the convergence. In addition to providing the optimization algorithm, we show that the grating-lobe-free beam-steering range of an antenna array can be extended by tilting the FoV. The novelty of this paper includes 1) application of the manifold optimization to reactive scatterer synthesis, 2) demonstration that the beam-steering range can be extended by tilting the FoV, and 3) introduction of a connected patch-diamond array antenna topology.

The framework for optimization, including objective function definitions, algorithm specifications, and gradient of the objective function, is described in Section II. In Section III, we present the design goals of this work and introduce the grating-lobe-free window's (GLFW's) tilting method for increasing the beam-steering range. Sections IV and V demonstrate the optimization and GLFW tilting methods with a 5-element linear patch-diamond array and a 4-by-4-element planar dual-polarized patch-diamond array.

II. OPTIMIZATION OF REACTIVE SCATTERERS
The concept behind the presented method is illustrated in Fig. 1. The optimization algorithm described in this section determines the terminations of the ports of the
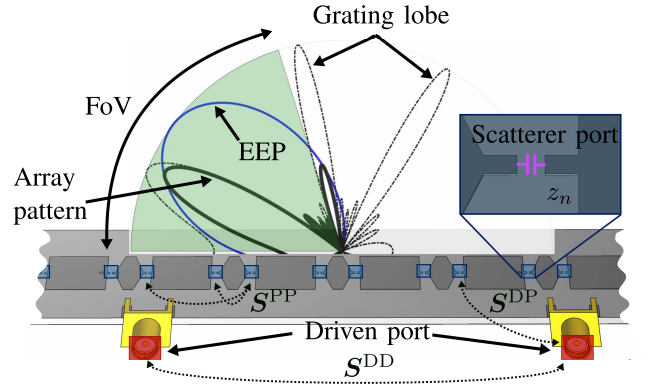

FIGURE 1. Conceptual view of the presented method. Red rectangles highlight the locations of driven ports, and blue rectangles show scatterer ports. Dashed arrows illustrate the coupling between the ports.
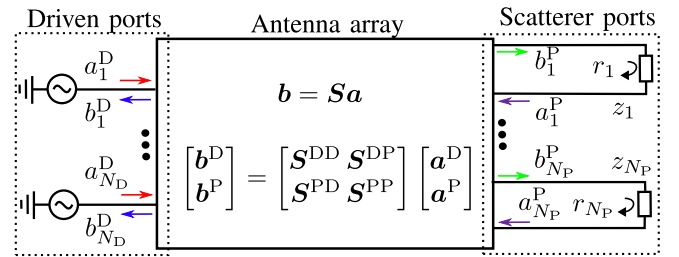

FIGURE 2. The N-port model of a passively loaded array antenna.

scatterer elements. In Fig. 1, a termination of the scatterer port n is visualized as a capacitor. The optimization goal, described in Section III, is to focus the EEPs excited by the driven ports toward the GLFW, which is highlighted as a green sector in Fig. 1. In the illustration, the GLFW is tilted to maximize the grating-lobe-free scan area. The dashed black pattern illustrates the array factor with grating lobes. The solid black line shows the radiation pattern of the array when the EEPs follow the blue curve.

A. MODEL OF PASSIVELY LOADED ANTENNA ARRAY
The passively loaded antenna array visualized in Fig. 2 contains N_D driven ports and N_P scatterer ports that are terminated to fixed impedance loads z_n, $n = 1 \cdots N_P$. The antenna is modeled using scattering parameters (S-parameters) that describe the ratios of the incident voltage waves a_n and coupled waves b_n. With superscript D, we refer to the driven ports, and P refers to the scatterer ports. The scattering matrix S is divided into blocks that describe the scattering between the driven ports (S^{DD}), between the driven and scatterer ports ($S^{DP} = (S^{PD})^T$), and between the scatterer ports (S^{PP}).

A full-wave electromagnetic simulation determines the S-parameters and the EEPs of each port. Assuming reference impedances in the ports, the total radiated field is a superposition of the EEPs of individual ports weighted by the complex feeding coefficients a_n.

Let r_n be the reflection coefficient in the scatterer port n, and $r \in \mathbb{C}^{N_P}$ denotes a vector of the reflection coefficients. As derived in [5], the incident waves into the scatterer ports after terminating the scatterer ports passively can be computed as

$$a^P = M^{-1} S^{PD} a^D, \tag{1}$$

where $M = R^{-1} - S^{PP}$ and $R = \text{diag}(r)$. Furthermore, the resulting scattering matrix that describes the ratios of the incident and coupled waves at the driven ports as $b^D = \hat{S} a^D$ can be computed as

$$\hat{S} = S^{DD} + S^{DP} M^{-1} S^{PD}. \tag{2}$$

Similarly, as the scatterer terminations affect the S-parameters, they affect the embedded element patterns of the driven elements. Let us define $e_{nl} \in \mathbb{C}$ as the EEP of port n toward direction (θ_l, φ_l) where the index $l \in [1, L]$ refers to a direction and polarization on a sphere. The polarization and direction-dependent component of the EEP is

$$e_{nl} = \vec{E}_n(\theta_l, \varphi_l) \cdot \vec{u}_{\alpha_l}, \tag{3}$$

where $\vec{E}_n(\theta_l, \varphi_l)$ is the electric far-field vector at (θ_l, φ_l) and $\vec{u}_{\alpha_l}$ is a unit vector that defines the polarization. In addition, let us define e_{nl}^D and e_{nl}^P as the EEPs of the driven and scatterer ports, respectively. After terminating the scatterer ports, the EEP of the driven port n is

$$\hat{e}_{nl} = e_{nl}^D + \left(s_n^{PD}\right)^T M^{-1} e_l^P. \tag{4}$$

Furthermore, the $N_D \times L$ -sized matrix containing the new EEPs is

$$\hat{E} = E^D + S^{DP} M^{-1} E^P. \tag{5}$$

B. OPTIMIZATION OBJECTIVE

The reflection coefficients of the scatterer ports, r, are the optimized parameters. In this paper, the optimization goal is to maximize the co-polarized realized gain of the antenna array's main beam within the grating-lobe-free beam-steering area. Nevertheless, the formulation would allow other optimization goals as well, including minimization of active reflection coefficients or minimization of the EEPs at undesired regions.

Let us define e_l^{tot} as the $\vec{u}_{\alpha_l}$-polarized electric far field radiated toward the direction (θ_l, φ_l) when the driven elements have feeding coefficients a_l. The realized gain of the full array can then be computed as

$$g_l = \frac{4\pi}{\eta} \frac{|e_l^{\text{tot}}|^2}{P_{\text{in}}} = \frac{4\pi}{\eta} \frac{|a_l^T \hat{e}_l|^2}{\|a_l\|_2^2}, \tag{6}$$

where P_{in} is the total incident power, η is the wave impedance, and $\|\cdot\|_2$ denotes the Euclidean norm. As proven in [27], for instance, the maximum realized gain is

$$\tilde{g}_l := \max_{a_l}(g_l) = \frac{4\pi}{\eta} \|\hat{e}_l\|_2^2, \tag{7}$$

and it is achieved if and only if $a_l \propto (\hat{e}_l)^*$, where $(\cdot)^*$ denotes element-wise complex conjugation.

Thus, the feeding coefficients do not need to be included in the optimization because they can be chosen optimally afterward. In the optimization, we maximize $\tilde{g}_l$ toward the desired directions. The optimization problem is

$$(P): \quad \underset{r \in \mathcal{C}}{\text{maximize}} \sum_{l=1}^{L} \sum_{n=1}^{N_D} |\hat{e}_{nl}|^2 = \|\hat{E}\|_F^2 \tag{8}$$

where $\|\cdot\|_F$ denotes the Frobenius norm. The feasible region $\mathcal{C}$ is addressed in the next section.

C. OPTIMIZATION ON RIEMANNIAN MANIFOLD

Because the scatterer ports are terminated to reactive loads, the magnitudes of the reflection coefficients are one in each scatterer port. In this case, the feasible region for the optimization variables is

$$\mathcal{C} = \{r \in \mathbb{C}^{N_P} : |r_n| = 1, \ \forall n = 1 \cdots N_P\}. \tag{9}$$

The region is a product of N_P complex unit circles and it is characterized as a smooth Riemannian manifold [17].

The problem is non-trackable in Euclidean space, which raises significant computational demands. Although convex relaxations could solve the problem, the solution might be practically non-realizable [19]. Therefore, we solve the problem intrinsically on the Riemannian manifold $\mathcal{C}$ rather than on the constant modulus-constrained Euclidean space.

The manifold-optimization methods have been detailed in [28] and [29]. The optimization is based on gradient descent algorithms, but rather than solving the next iterate based on the Euclidean gradient, the intrinsic Riemannian gradient defines the descent direction on the given manifold. The main steps of the algorithm on the manifold $\mathcal{C}$ have been described in [17].

In practice, we use the Manopt toolbox implemented in MATLAB [30], [31]. We use the Riemannian trust-regions solver (RTR), which has been explained in detail in [32]. We approximate the Hessian operator with finite differences, as explained in [33]. The manifold $\mathcal{C}$ is denoted as `complexcirclefactory` in the Manopt toolbox [30].

The optimization is gradient-based, and the convergence can be significantly improved by providing an analytically calculated gradient vector instead of automatic differentiation [30]. In our problem setting, an element n of the Euclidean gradient vector $\nabla \|\hat{E}\|_F^2 \in \mathbb{C}^{N_P}$ is

$$\frac{\partial \|\hat{E}\|_F^2}{\partial r_n} = 2 \, \text{trace}\left((\hat{E}_n')^H \hat{E}\right), \tag{10}$$

where

$$\hat{E}_n' = -S^{DP} M^{-1} \frac{\partial M}{\partial r_n^{\text{Re}}} M^{-1} E^P. \tag{11}$$

The reflection coefficients are divided into real and imaginary parts as $r_n = r_n^{\text{Re}} + j r_n^{\text{Im}}$, where j is the imaginary unit.

An element of the partial derivative of $\boldsymbol{M}$ with respect to r_n^{Re} at row i and column j is

$$\left(\frac{\partial \boldsymbol{M}}{\partial r_n^{\text{Re}}}\right)_{ij} = \delta_{ijn} \frac{1}{(r_n^{\text{Im}} - jr_n^{\text{Re}})^2}, \tag{12}$$

where δ_{ijl} is the Kronecker delta function. The intrinsic Riemannian gradient is computed in Manopt by projecting the Euclidean gradient onto the tangent space of $\mathcal{C}$. The projection operator for this manifold is given in [17].

III. MAXIMAL GRATING-LOBE-FREE FIELD OF VIEW

In this section, we demonstrate that tilting the antenna array's field of view can increase the available beam-steering area. Sparse antenna arrays with inter-element distances larger than half of a wavelength introduce grating lobes. To mitigate the grating lobes, the antenna array's field of view must be limited to the grating-lobe-free window. That is done by maximizing the radiated power for the beams inside the GLFW, that is, maximizing (7) for (θ_l, φ_l) inside the GLFW. Consequently, the radiation outside of the GLFW is decreased since the total input power is constant.

We consider antenna arrays that have a rectangular lattice configuration and inter-element distances d_x and d_y in x and y-directions in Cartesian coordinates. Let us define the uv-plane as

$$u = \sin\theta\cos\varphi, \tag{13}$$

$$v = \sin\theta\sin\varphi, \tag{14}$$

where $\theta \in [-90°, 90°]$, $\varphi \in [0°, 180°]$ are the spherical coordinates of the half space. On the uv-plane, the grating lobes occur at directions

$$u_{\text{GL}} = u_{\text{MB}} - p\frac{\lambda}{d_x}, \tag{15}$$

$$v_{\text{GL}} = v_{\text{MB}} - q\frac{\lambda}{d_y}, \tag{16}$$

where $(u_{\text{MB}}, v_{\text{MB}})$ is the main-beam direction, λ is wavelength, and $p, q = \pm 1, \pm 2, \ldots$ [34].

The grating-lobe-free window can be determined based on the grating-lobe locations. The GLFW is defined by the uv coordinates that satisfy

$$|u_0 - u| < \frac{\lambda}{2d_x}, \tag{17}$$

$$|v_0 - v| < \frac{\lambda}{2d_y}, \tag{18}$$

$$u^2 + v^2 < 1, \tag{19}$$

where (u_0, v_0) is the center point of the GLFW. On the uv-plane, the GLFW is a $\lambda/d_x \times \lambda/d_y$-sized rectangle without dependency on u_0 and v_0 if the rectangle is fully inside the unit circle on the uv-plane. Otherwise, the GLFW is the part of the particular rectangle inside the circle. However, the size of the GLFW on the spherical shell defines the antenna
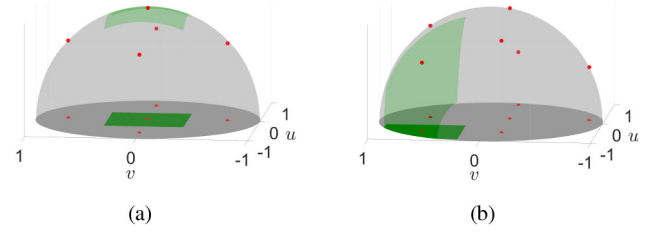

FIGURE 3. Planar array GLFWs on the uv-plane and projected on the spherical shell. The main beam and grating lobes have been illustrated as red dots. The array in (a) has a broadside-located GLFW, and that in (b) has a tilted GLFW.

array's scan area. When the GLFW is projected from the uv-plane onto the sphere, its size depends on its position (u_0, v_0).

Figure 3 demonstrates the GLFW tilting method for a case in which the inter-element distances are $d_x = d_y = 1.4\,\lambda$. The GLFWs are plotted on both the uv-plane and on the sphere. In addition, the locations of the grating lobes and the main beam are indicated as red dots. The main beam is steered to the center of the GLFW.

The broadside-located GLFW in Fig. 3(a) covers 8.5% of the half-sphere area. In Fig. 3(b), the GLFW is tilted to the direction $(u_0, v_0) = (-0.562, 0.562)$. The size of the GLFW on the sphere is then 14% of the half-sphere area. The tilted direction is chosen so that $u_0 = -v_0$, and the area of the GLFW on the sphere is maximized. Even if the GLFW is partly outside of the visible range (uv unit circle), the scan coverage area is increased by 65%.

For arrays with rectangular lattices, the GLFW is also a rectangle. By using different lattices, such as spherical or hexagonal, the GLFWs would have different shapes, which could benefit certain practical applications [2]. However, lattices other than rectangular ones are excluded from the scope of this work.

To limit the scan area into the GLFW, the EEPs should be maximized toward the GLFW and minimized elsewhere. We study a linear 5-element array with 1.4-λ inter-element distances. The EEPs have been formed analytically so that the EEP of each element n follows the curve

$$e_n(\theta) = \frac{1}{N_{\text{D}}}\cos^\kappa(\theta - \theta_0), \tag{20}$$

where θ_0 is the center point of the GLFW, and

$$\kappa = -1/\log_2(\cos(\Delta\theta/2)), \tag{21}$$

where $\Delta\theta$ is the angular width of the GLFW. Thus, the EEPs' half-power beam widths equal the width of the GLFW.

Figure 4 illustrates the analytically formed EEP, the array factor, and the array radiation pattern with a randomly selected scan direction in linear scale. In addition, the GLFWs are highlighted as green sectors. If the EEPs were omnidirectional, the array factor would equal the total radiation pattern. However, because the EEPs limit the radiation pattern into the GLFW, the radiation is minimized outside of the GLFW.
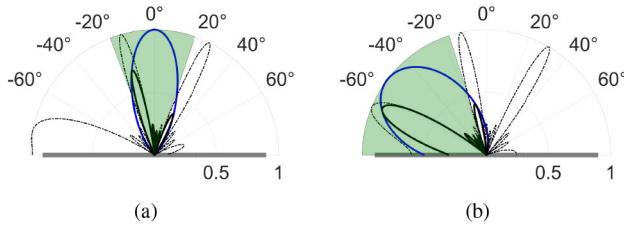
FIGURE 4. Grating-lobe-free scan areas of the linear array. The array factor is illustrated in the dashed black line, the normalized EEPs in the blue line, and the radiation pattern of the array in the black solid line. The array in (a) has a broadside located GLFW, and the array in (b) has a tilted GLFW.

TABLE 1. Dimensional parameters of the linear array.

Parameter	W_{tot}	L_{tot}	W_p	L_p	W_s	W_{sp}	W_c	L_c
Value (mm)	420	40	12	15	2	1.7	0.5	0.7

With the linear array, the scan area can also be increased by tilting the GLFW. Without tilting, the angular width of the scan area is $\Delta\theta = 41.8°$. When the GLFW is tilted so that its center direction is $\theta_0 = -53.3°$, the angular width of the GLFW is $\Delta\theta = 73.4°$. The calculated scanning areas are presented in Fig. 4.

Figure 4 is also animated in GIF videos provided as supplementary material. The beam-steering animation of the array with the broadside-located GLFW is animated in the file *beamsteering_analytical_broadside.gif*, and the tilted case is animated in *beamsteering_analytical_tilted.gif*.

IV. DEMONSTRATION USING LINEAR PATCH-DIAMOND ARRAY

We optimize the scatterer terminations for two cases. The first goal is to synthesize an array with a broadside-located GLFW. In the second case, the GLFW is tilted. In both cases, we use the same antenna topology and simulation data. The simulations are performed using CST Studio Suite [35]. Both antenna arrays of the two cases are finally manufactured and characterized by measurements.

A. ANTENNA STRUCTURE

The method is tested at a 5-GHz point frequency. The studied antenna is a 5-element, patch-diamond-shaped PCB antenna array with 1.4-λ inter-element distances as shown in Fig. 5. 40 scatterer components are placed between the patches and the diamonds. The port numbering is ascending towards the positive x-axis and starts from one in both driven and scatterer ports.

The most important dimensions of the antenna are marked in Fig. 5 and described in Table 1. The radius of vias, which are illustrated in Fig. 5(b) and Fig. 5(c), is 0.5 mm. The substrate is 1.524-mm-thick Rogers Ro4360G2.

The model of the connector, which is highlighted in yellow, is Molex 0732511150. The connectors are modeled in the simulation, and the excitations of the driven elements are at the apertures of the connectors. The transmissions from the connectors to the patches are implemented using curvy coplanar waveguides, which are illustrated in Fig. 5(b).
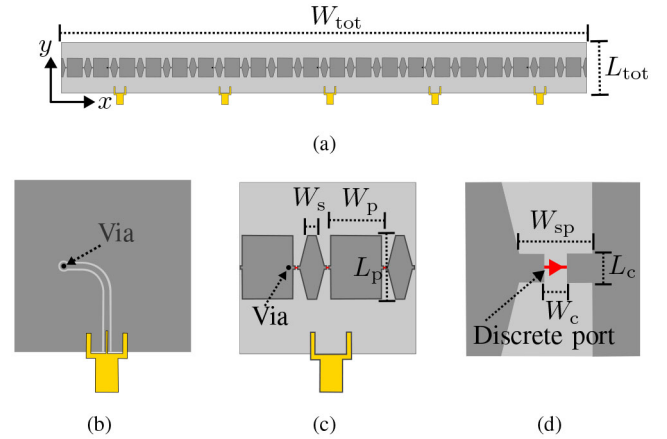

FIGURE 5. Simulation model of the linear patch-diamond array. Light gray represents the substrate material, dark gray represents copper, and yellow represents a feeding connector. Red markers show the locations of the scatterer ports. (a) Full antenna array and coordinate axes. (b) Zoomed-in view of the bottom copper layer. (c) Zoomed-in view of top copper. (d) Visualization of a scatterer port location.

Figure 5(d) shows the location of a scatterer port. In the simulation, the discrete port is aligned from copper edge to edge. The sizes of the port gap and pads are chosen so that a component of size 0402 fits well there.
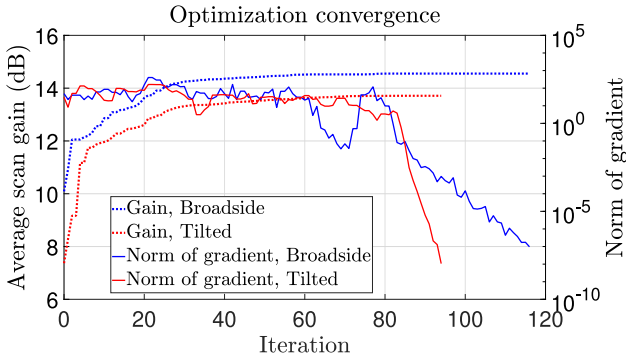
The antenna array's topology is designed by considering the following insights. First, the driven ports should exhibit satisfactory impedance matching in the case in which the other ports are terminated to the generator impedances, as the scatterer terminations have limited influence on the driven ports' input impedances. Second, strong coupling between the driven ports and scatterer ports is essential. Without sufficient coupling, the waves coupled to scatterer ports would have no significant effect.

The third observation is that all ports should radiate well to the desired directions, which can be located at the broadside or tilted sector. Using the patch-diamond structure shown in Fig. 5, the ports radiate sufficiently to both broadside and tilted directions. Lastly, the array's five elements are interconnected rather than isolated. This configuration enables each element to generate electric current distribution across the entire structure rather than being limited to its individual space. This concept proves advantageous for arrays with limited FoV because a large element aperture enables effective shaping of the EEP.

In the simulation, the scatterer ports are fed by 50-Ω discrete ports. The driven ports are excited by 50-Ω waveguide ports. The aim is to solve S-parameters and EEPs related to all ports of the model. After obtaining the data from the simulation, we use the algorithm described in Section II to optimize the terminations for the scatterer ports so that the gain is maximized towards the GLFW. The optimization method and the goal are defined more precisely in the following subsection.

TABLE 2. θ coordinates of the objective direction grid.

l	θ_l, Broadside	θ_l, Tilted
1	-21°	-90°
2	-16°	-82°
3	-12°	-74°
4	-7°	-66°
5	-2°	-57°
6	2°	-49°
7	7°	-41°
8	12°	-33°
9	16°	-25°
10	21°	-17°

FIGURE 6. Convergence of the optimization algorithm with the linear antenna array.

TABLE 3. List of selected capacitors (*C*) and inductors (*L*), and the ports in which the components are placed in the prototypes.

C (pF)	L (nH)	Ports, broadside	Ports, tilted
0.1		37	1, 6, 14, 16, 22, 24, 30, 32, 38
0.2		1, 8, 9, 11, 16, 17, 19, 24, 25, 32, 33, 35	4, 12, 28, 36
0.3		3, 27,	20
0.7		7, 15, 23, 28, 31	
0.8		2, 10, 18	5, 13, 21, 23, 29, 37
0.9		26, 34, 36	15, 31
1.1			7
1.2			19, 27
1.3			2, 39
1.4		39	
1.5			11
1.6		20	35
2.6		5	
2.7			3
3.7		12	
4.1		29, 38	
4.7		13	
8.1			10
15			34
27		21	
	0.8		18, 26
	1.7	4	25
	1.8		17
	2.4	30	
	2.5		33
	3.5		9
	3.8	22	
	4.3	40	
	5.7	14	
	7.2	6	
	9.2		40
	36		8

B. OPTIMIZATION PROCESS

The optimization algorithm is implemented using MATLAB and Manopt. The broadside GLFW is located at $\varphi = 0°$, $\theta \in [-21°, 21°]$, and the tilted GLFW at $\theta \in [-90°, -17°]$. The cases are the same as those illustrated in Section III.

We solve the problem defined in (8). The feasible region is the manifold defined in (9). The Euclidean gradient of the objective function is computed using (10). The co-polarization $\vec{u}_{\alpha_l}$ is chosen based on Ludwig's third definition of cross-polarization due to the orientation of the array [36]. The objective grid, that is, the set $\{(\theta_l, \varphi_l)\}_{l=1}^{L}$, is defined so that for all l, $\varphi_l = 0$, and there is fixed spacing between θ angles. Table 2 describes the objective grid for both broadside and tilted cases.

The optimization problems for the two cases are solved using the RTR solver in the Manopt toolbox with initial guess $r^{(0)} : r_n^{(0)} = 1, \forall n$. The solver parameters $\bar{\Delta}$ and Δ_0, discussed in [32], are obtained automatically by the Manopt toolbox based on the given problem setting, and ρ' is set to the Manopt's default value ($\rho' = 0.1$) [30].

Figure 6 studies the convergence of the optimization and shows the average realized gain and the norm of the intrinsic gradient of the objective function as a function of the iteration number. The optimization algorithm terminates when the norm of the intrinsic gradient vector falls below 10^{-7}. In the broadside case, the optimization converges after 116 iterations. The total time elapsed in the optimization process is roughly one minute. In the tilted case, the number of iterations is 94, and the time elapsed is approximately 30 seconds.

After the optimization, the optimal reflection coefficients are implemented using realistic reactive components. The available component library includes Murata's GJM15 capacitor set and Coilcraft's 0402DC inductor set. The components are chosen based on the S-parameter data of the components provided by the component manufacturers. The used components are listed in Table 3.

C. PROTOTYPING RESULTS

Prototypes of the two reactively loaded antenna arrays have been manufactured. In addition, a third prototype without
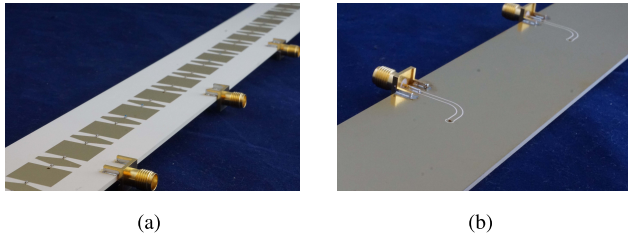
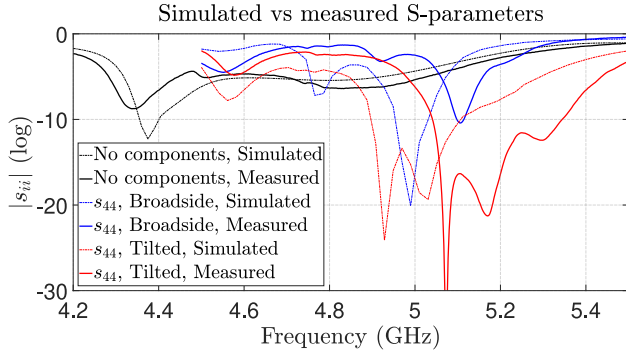**FIGURE 7.** Manufactured prototype. (a) Top view. (b) Bottom view.

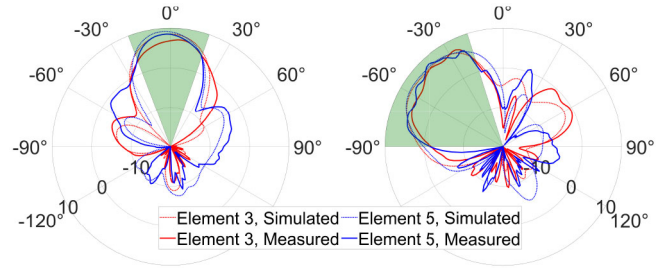**FIGURE 8.** Passive S-parameters of the three prototypes.

FIGURE 9. Measured and simulated co-polarized EEPs in the dB scale of the center and edge elements of the broadside and tilted arrays. The GLFWs are highlighted in the green sector.

FIGURE 10. Embedded realized gain patterns of all elements and maximum scan gains. Green areas illustrate the GLFWs. (a) Broadside array. (b) Tilted array.

components, containing only the middle connector (at driven port number 3), has been manufactured for reference. Figure 7 shows the final tilted-GLFW prototype.

The S-parameters of the three prototypes are measured using the vector network analyzer (VNA) and compared to simulated results, which are computed using (2). Figure 8 illustrates the s_{44} parameters of the manufactured and simulated devices.

Figure 8 shows that the resonant frequencies of the two reactively loaded arrays have shifted by 150 MHz. Sources for this include manufacturing, simulation, and material property inaccuracies. However, the main factor is the uncertainty in the values of the surface-mounted components, because the error is small in the third reference prototype. The S-parameters provided by the component manufacturers often differ drastically from the realized S-parameters [37], which explains the frequency shift in this case.

The EEPs of the manufactured prototypes are measured using the MVG StarLab 6 GHz spherical near-field scanner [38] at 5.15 GHz. Figure 9 illustrates the simulated and measured EEPs of the driven elements 3 and 5 of the broadside and tilted arrays. The simulated patterns are computed using (4). The curves show the partial realized gain of the elements when the other elements are terminated to their generator impedances (50 Ω). The measured results exhibit satisfactory correspondence with the simulations.

Figure 10 shows the measured embedded partial realized gain patterns of all elements, as well the maximum scan gain, computed using (7). The bold sections of the curves highlight the portions at which the magnitudes are above −3 dB of their maxima. In the broadside prototype, the −3 dB scan window is from −16° to 20°, and in the tilted prototype,
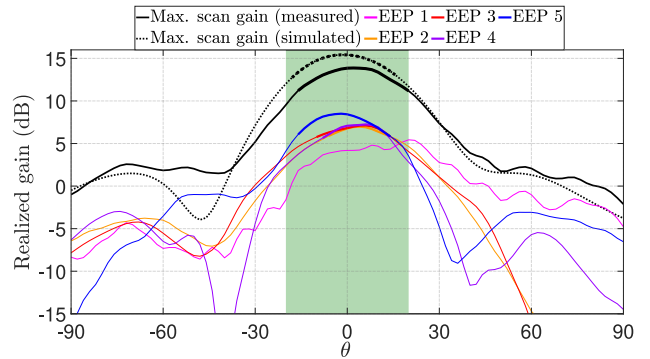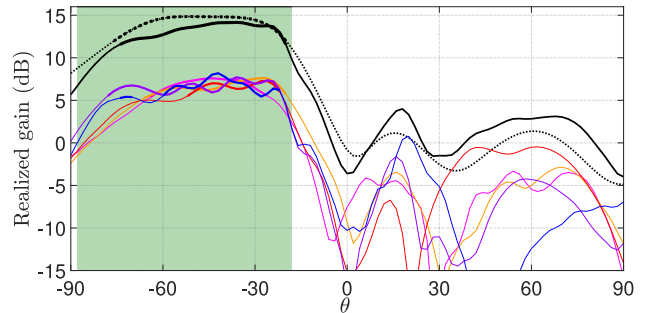
it is from −74° to −20°. That is, the angular width of the 3-dB scan window is 50 % larger in the tilted array than in the broadside array.

The simulated partial realized scan gain of the broadside array is 15.4 dB when the beam is steered to $(\theta, \varphi) = (0°, 0°)$. The corresponding measured gain is 13.8 dB. In the tilted array, the simulated partial realized scan gain is 14.8 dB when the beam is steered to $(\theta, \varphi) = (−54°, 0°)$. The corresponding measured gain is 13.4 dB.

The beam-steering capabilities of the measured arrays are animated in supplementary GIF videos *beamsteering_measured_broadside.gif* and *beamsteering_measured_tilted.gif*. The animations demonstrate the beam steering inside the GLFWs in broadside and tilted cases, respectively.
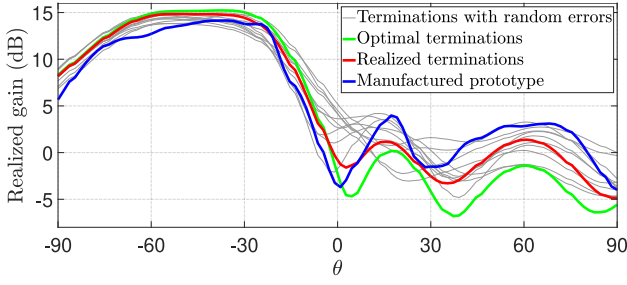
FIGURE 11. Effect of component errors and quantization errors on the resulting scan gain of the tilted array.

The discrete values of the surface-mounted components do not match exactly with the optimal values. In addition, the components themselves introduce errors in their values. Figure 11 presents an analysis of the degree to which the component errors and the quantization errors affect the resulting total scan gain of the tilted array. The component errors are set randomly within the tolerances reported by the component manufacturers.

Quantization does not significantly reduce the gain. However, the component errors might affect even several decibels. The errors could be mitigated by replacing the surface-mounted components with inter-digital capacitors and inductive meandered lines realized on the same printed circuit board together with the antenna, which could also enable application of the method for higher frequencies.

V. DEMONSTRATION USING PLANAR DUAL-POLARIZED ARRAY

The feasibility of the method for larger problems is further demonstrated with a 4-by-4-element, dual-polarized planar array. The planar array is reactively loaded to operate either in the broadside FoV or in the tilted FoV. This test antenna is analyzed only by simulations.
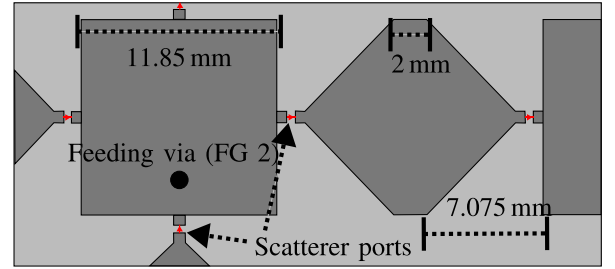
A. SIMULATED ANTENNA STRUCTURE

Figure 12 presents the test structure, similar to the previous structure but enlarged to two dimensions. The inter-element distances are 1.4λ in both x- and y-directions. Figure 12(b) shows the main dimensions of the patches and diamonds. The scatterer port dimensions and the sizes of component pads are the same as those in the linear array, and they are shown in Fig. 5(d). The driven ports are located at the ground plane so that the ports are placed between the vias and the ground plane.

Each element in the planar array consists of 9 patches and 12 full diamonds. The number of scatterer ports in each element is 36, which results in 576 scatterer ports in the full array. Each element has two driven ports, whose EEPs are designated to have orthogonal polarizations. Thus, dual-polarized operation can be achieved. The driven ports are divided into feeding groups (FGs) 1 and 2. Feeding group 1 is specified to radiate Ludwig 3 cross-polarization, and FG 2 should radiate Ludwig 3 co-polarization. In Fig. 12(a), the
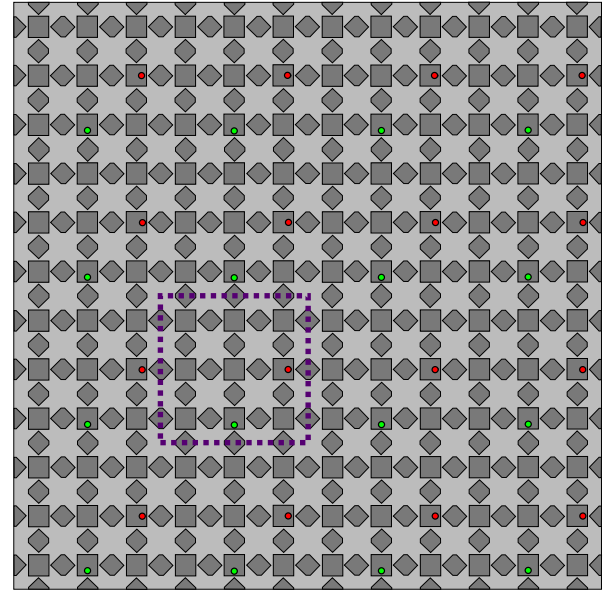
(a)

(b)

FIGURE 12. Simulation model of the dual-polarized planar antenna array. (a) Full array with driven ports marked as red (FG 1) and green (FG 2) dots. The dashed line highlights an element. (b) Zoomed-in view of the structure and the main dimensions.

ports of FG 1 and 2 are marked as red and green dots, respectively.

B. OPTIMIZATION PROCESS

The reactive components are optimized for the broadside and tilted GLFWs. The GLFWs are the same as those shown in Fig. 3. The center point of the tilted GLFW is at $(u_0, v_0) = (-0.562, 0.562)$ which corresponds to the direction $(\theta_0, \varphi_0) = (53°, 135°)$ on the sphere. The objective direction grids are illustrated in Fig. 13. The broadside GLFW includes 16 directions, and the tilted GLFW includes 24 directions.

In this case, the objective function of the optimization is a sum of the two objectives defined by the feeding groups. That is, the optimization problem is

$$\underset{r \in \mathcal{C}}{\text{maximize}} \sum_{l \in \mathcal{L}_1} \sum_{n \in \mathcal{N}_1} |\hat{e}_{nl}(\boldsymbol{r})|^2 + \sum_{l \in \mathcal{L}_2} \sum_{n \in \mathcal{N}_2} |\hat{e}_{nl}(\boldsymbol{r})|^2, \quad (22)$$
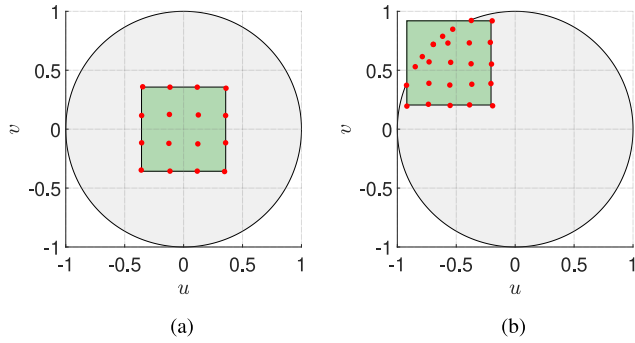
FIGURE 13. Planar array objective direction grids. Red dots indicate the grid points on the *uv* plane, and the rectangles indicate the GLFWs. (a) Broadside array. (b) Tilted array.
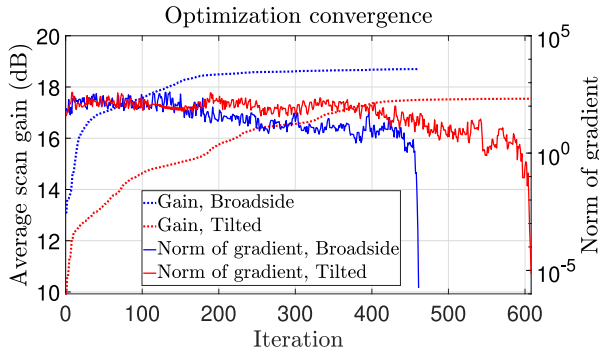

FIGURE 14. Convergence of the optimization algorithm with the planar antenna array.

where the $\hat{e}_{nl}(\boldsymbol{r})$ is the embedded element pattern of the driven port n to the direction and polarization l after terminating the scatterer ports to the reflection coefficients $\boldsymbol{r}$. $\hat{e}_{nl}(\boldsymbol{r})$ is computed using (4). The gradient of this objective function is computed based on (10). The index sets $\mathcal{L}_1$ and $\mathcal{L}_2$ contain the indices of the target directions shown in Fig. 13 with Ludwig 3 cross and co-polarization, respectively. Correspondingly, the index sets $\mathcal{N}_1$ and $\mathcal{N}_2$ contain the indices of the ports of the feeding groups 1 and 2, respectively.

The solver parameters, as well as the initial guess, are selected similarly as with the linear array. Figure 14 shows the convergence of the optimization algorithm. In the broadside case, the optimization converges after 462 iterations taking approximately 7 hours. In the tilted case, the number of iterations is 610, and the elapsed time is 14 hours.

C. SIMULATION RESULTS

The optimal reflection coefficients are implemented using the components from the available component library. Figure 15 shows the maximum realized partial scan gain of the broadside array. The contours show the main beam realized partial gain when the beam is steered with the optimal feeding coefficients toward the direction given in *uv* coordinates. The gain is normalized so that the maximum co-polarized gain is 0 dB. Thus, the −3-dB contour shows
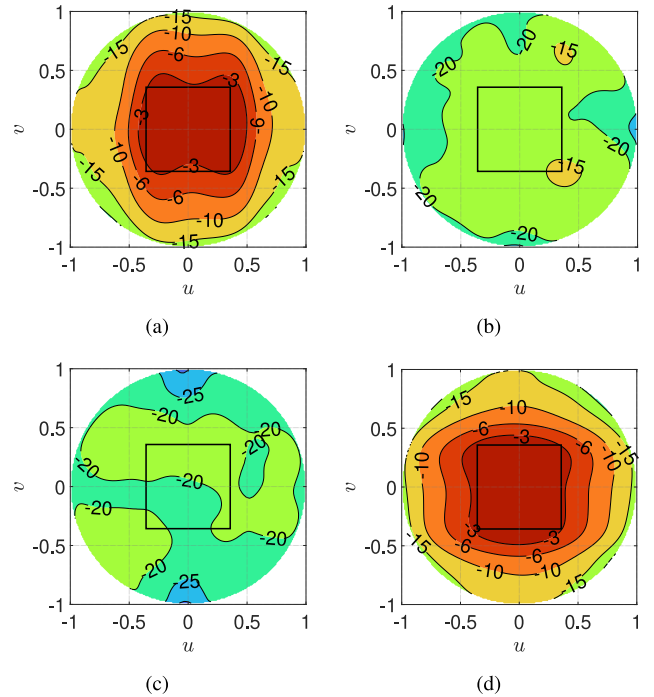

FIGURE 15. Maximum partial realized scan gain of the broadside array in the normalized dB scale. The rectangle shows the GLFW. (a) and (b): Ludwig 3 cross- and co-polarizations, respectively, of FG 1. (c) and (d): Ludwig 3 cross- and co-polarizations, respectively of FG 2.

FIGURE 16. Maximum partial realized scan gain of the tilted array in the normalized dB scale. The rectangle shows the GLFW. (a) and (b): Ludwig 3 cross- and co-polarizations, respectively, of FG 1. (c) and (d): Ludwig 3 cross- and co-polarizations, respectively of FG 2.
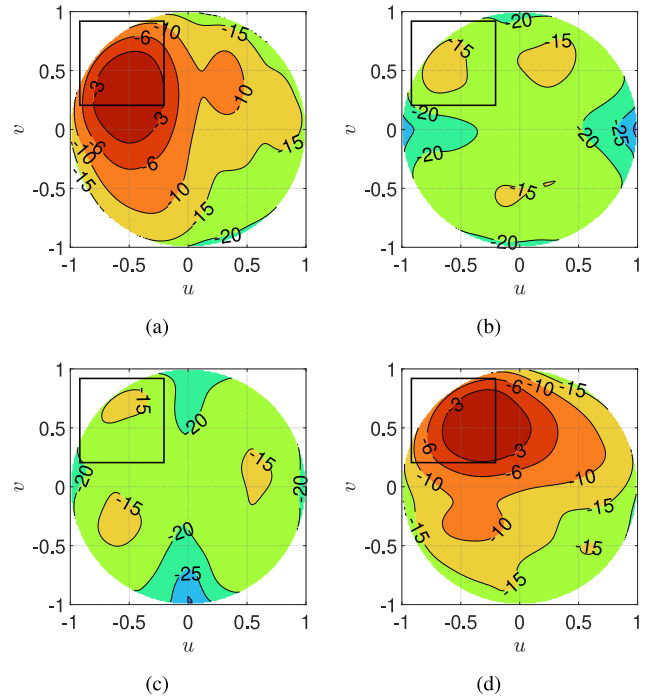
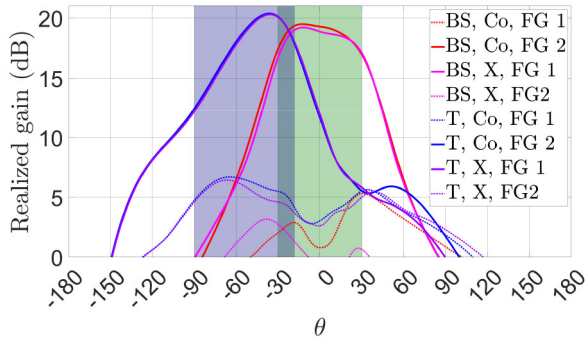the 3-dB scan area. Fig. 16 shows the same illustrations for the tilted array.

FIGURE 17. Partial realized scan gain envelopes on a $\varphi = 135°$ diagonal plane. Results for tilted (T) and broadside (BS), Ludwig 3 co-polarization (Co), and cross-polarization (X) are indicated. The sectors highlight broadside and tilted GLFWs.

The broadside array's results show that the 3-dB scan area covers the GLFW nearly completely. The coverage is similar for both polarizations. However, the coverage areas of FG 1 and FG 2 of the tilted array do not overlap completely, and the 3-dB areas do not fully cover the GLFW. In all cases, the cross-polarization levels are below -10 dB compared to maximum scan gain.

Figure 17 shows the maximum realized partial scan gain on the diagonal plane $\varphi = 135°$. The GLFWs are marked as well. Fig. 17 shows the scan gain without normalization. The peak scan gain of the broadside array is 19.8 dB for both feeding groups. The peak scan gain of the tilted array is 20.8 dB for both feeding groups. The curves indicate satisfactory dual-polarized performance, as the curves of FG 1 and FG 2 match well. The broadside array produces a flatter and thus more useful gain pattern compared to the tilted array.

VI. CONCLUSION

This paper introduced a novel manifold optimization-based approach for designing reactively loaded sparse antenna arrays, particularly tailored for applications with limited field of view. In addition, we demonstrated that the grating-lobe-free scan range can be extended by tilting the field of view. The proposed algorithm was successfully demonstrated in the design process of antenna arrays, using innovative patch-diamond-shaped configurations. The results illustrated that antenna arrays can be synthesized to radiate towards either broadside-located or tilted grating-lobe-free windows without a significant decrease in scan gain. The results are particularly relevant at high frequencies, at which the tightly integrated large RFICs necessitate large inter-element distances.

REFERENCES

[1] B. Sadhu, X. Gu, and A. Valdes-Garcia, "The more (antennas), the merrier: A survey of silicon-based mm-wave phased arrays using multi-IC scaling," *IEEE Microw. Mag.*, vol. 20, no. 12, pp. 32–50, Dec. 2019.

[2] S. P. Skobelev, *Phased Array Antennas with Optimized Element Patterns*. Artech House, Norwood, MA, USA, 2011.

[3] S. P. Skobelev, "Methods of constructing optimum phased-array antennas for limited field of view," *IEEE Antennas Propag. Mag.*, vol. 40, no. 2, pp. 39–49, Apr. 1998.

[4] S. P. Skobelev and I. A. Makeev, "Some features of shaping narrow flat-topped radiation patterns by overlapped subarrays in limited-scan waveguide phased array antennas," in *Proc. 11th Eur. Conf. Antennas Propag. (EuCAP)*, 2017, pp. 1101–1105.

[5] R. T. Maximidis, D. Caratelli, G. Toso, and A. B. Smolders, "Design of overlapped subarrays based on aperture reactive loading," *IEEE Trans. Antennas Propag.*, vol. 68, no. 7, pp. 5322–5333, Jul. 2020.

[6] D. Petrolati, P. Angeletti, and G. Toso, "A lossless beam-forming network for linear arrays based on overlapped sub-arrays," *IEEE Trans. Antennas Propag.*, vol. 62, no. 4, pp. 1769–1778, Apr. 2014.

[7] N. Singhal and S. M. R. Hasan, "Review and comparison of different limited scan phased array antenna architectures," *Int. J. Circuit Theory Appl.*, vol. 49, no. 10, pp. 3111–3130, 2021.

[8] R. Kormilainen, A. Lehtovuori, and V. Viikari, "A method for tailoring the gain pattern of a single antenna element," *IEEE Open J. Antennas Propag.*, vol. 2, pp. 431–438, 2021.

[9] R. Harrington, "Reactively controlled directive arrays," *IEEE Trans. Antennas Propag.*, vol. 26, no. 3, pp. 390–395, May 1978.

[10] F. Fezai, C. Menudier, M. Thevenot, and T. Monediere, "Systematic design of parasitic element antennas—Application to a WLAN Yagi design," *IEEE Antennas Wireless Propag. Lett.*, vol. 12, pp. 413–416, 2013.

[11] R. Lamey, M. Thevenot, C. Menudier, E. Arnaud, O. Maas, and F. Fezai, "Interleaved parasitic arrays antenna (IPAA) for active VSWR mitigation in large phased array antennas with wide-angle scanning capacities," *IEEE Access*, vol. 9, pp. 121015–121030, 2021.

[12] R. Harrington and J. Mautz, "Control of radar scattering by reactive loading," *IEEE Trans. Antennas Propag.*, vol. 20, no. 4, pp. 446–454, Jul. 1972.

[13] F. Jiang et al., "Pixel antenna optimization based on perturbation sensitivity analysis," *IEEE Trans. Antennas Propag.*, vol. 70, no. 1, pp. 472–486, Jan. 2022.

[14] J. Córcoles, "Reactively loaded array pattern synthesis as a quadratically constrained quadratic program," *IEEE Trans. Antennas Propag.*, vol. 63, no. 11, pp. 5219–5224, Nov. 2015.

[15] R. Kormilainen, A. Lehtovuori, J. Liesiö, and V. Viikari, "A method to co-design antenna element and array patterns," *IEEE Access*, vol. 10, pp. 31190–31200, 2022.

[16] B. Fuchs, "Application of convex relaxation to array synthesis problems," *IEEE Trans. Antennas Propag.*, vol. 62, no. 2, pp. 634–640, Feb. 2014.

[17] K. Alhujaili, V. Monga, and M. Rangaswamy, "Transmit MIMO radar beampattern design via optimization on the complex circle manifold," *IEEE Trans. Signal Process.*, vol. 67, no. 13, pp. 3561–3575, Jul. 2019.

[18] K. Zhong, J. Hu, C. Pan, X. Yu, and X. Li, "MIMO radar beampattern design based on manifold optimization method," *IEEE Commun. Lett.*, vol. 26, no. 5, pp. 1086–1090, May 2022.

[19] K. Zhong, J. Hu, Y. Cong, G. Cui, and H. Hu, "RMOCG: A Riemannian manifold optimization-based conjugate gradient method for phase-only beamforming synthesis," *IEEE Antennas Wireless Propag. Lett.*, vol. 21, pp. 1625–1629, 2022.

[20] S. Yatawatta, "Radio interferometric calibration using a Riemannian manifold," in *Proc. IEEE Int. Conf. Acoust. Speech Signal Process.*, 2013, pp. 3866–3870.

[21] M. A. Nazari, G. Seco-Granados, P. Johannisson, and H. Wymeersch, "3D orientation estimation with multiple 5G mmWave base stations," in *Proc. IEEE Int. Conf. Commun.*, 2021, pp. 1–6.

[22] H. Guo, Y.-C. Liang, J. Chen, and E. G. Larsson, "Weighted sum-rate maximization for reconfigurable intelligent surface aided wireless networks," *IEEE Trans. Wireless Commun.*, vol. 19, no. 5, pp. 3064–3076, May 2020.

[23] I. A. Luchnikov, A. Ryzhov, S. N. Filippov, and H. Ouerdane, "QGOpt: Riemannian optimization for quantum technologies," *SciPost Phys.*, vol. 10, p. 79, Mar. 2021.

[24] N. D. Nguyen, J. Huang, and D. Wang, "A deep manifold-regularized learning model for improving phenotype prediction from multi-modal data," *Nat. Comput. Sci*, vol. 2, no. 1, pp. 38–46, 2022.

[25] A. Majumdar, G. Hall, and A. A. Ahmadi, "Recent scalability improvements for semidefinite programming with applications in machine learning, control, and robotics," *Annu. Rev. Control Robot. Autonomous Syst.*, vol. 3, no. 1, pp. 331–360, 2020.

[26] S. K. Roy, Z. Mhammedi, and M. Harandi, "Geometry aware constrained optimization techniques for deep learning," in *Proc. IEEE Comput. Soc. Conf. Comput. Vis. Pattern Recognit.*, 2018, pp. 4460–4469.

[27] A. Salmi, A. Lehtovuori, and V. Viikari, "On realized gain-optimal feeding coefficients of antenna arrays," in *Proc. 17th Eur. Conf. Antennas Propag. (EuCAP)*, Florence, Italy, 2023, pp. 1–5.

[28] P.-A. Absil, R. Mahony, and R. Sepulchre, *Optimization Algorithms on Matrix Manifolds*. Princeton, NJ, USA: Princeton Univ. Press, 2008.

[29] N. Boumal, *An Introduction to Optimization on Smooth Manifolds*. Cambridge, U.K.: Cambridge Univ. Press, 2023.

[30] N. Boumal, B. Mishra, P.-A. Absil, and R. Sepulchre, "Manopt, a MATLAB toolbox for optimization on manifolds," *J. Mach. Learn. Res.*, vol. 15, no. 42, pp. 1455–1459, 2014. [Online]. Available: https://www.manopt.org

[31] *MATLAB: Version 9.14.0.2239454 (R2023a)*. Natick, MA, USA: The MathWorks Inc., 2023.

[32] P.-A. Absil, C. G. Baker, and K. A. Gallivan, "Trust-region methods on Riemannian manifolds," *Found. Comput. Math.*, vol. 7, no. 3, pp. 303–330, Jul. 2007.

[33] N. Boumal, "Riemannian trust regions with finite-difference hessian approximations are globally convergent," in *Proc. Int. Conf. Geom. Sci. Inf.*, 2015, pp. 467–475.

[34] P.-S. Kildal, *Foundations of Antenna Engineering: A Unified Approach for Line-of-Sight and Multipath*. Artech House, Norwood, MA, USA, 2015.

[35] "CST studio suite." Dassault Systems. Accessed: Aug. 2023. https://www.3ds.com/products-services/simulia/products/cst-studio-suite/

[36] A. Ludwig, "The definition of cross polarization," *IEEE Trans. Antennas Propag.*, vol. 21, no. 1, pp. 116–119, Jan. 1973.

[37] S. Skidmore, L. Levesque, S. Muir, J. Boh, and H. Siang, "Understanding S-parameter vs. equivalent circuit-based models for RLC component simulations in Keysight ADS and Genesys," Modelithics, Tampa, FL, USA, Apr. 2014. [Online]. Available: https://www.modelithics.com/FreeDownloads/WhitePapers/WhPaper_Equiv_Circuit_Model_Note_Final_ADS.pdf

[38] (MVG, Paris, France). *StarLab 6 GHz Spherical Near-Field Scanner*. Accessed: Aug. 2023. https://www.mvg-world.com/en/products/antenna-measurement/multi-probe-systems/starlab